Design and implementation of a gliding cross-domain vehicle

Yucheng Zou [b], Chenxi You [a], Xiangkui Tan [a], Yiwei Wang [d,e], Jingzhu Wang [d], Chaohui Li [b], Ming He [a], Kai Lv [a], Yong Zou [b], Huaitong Song [a], Pengyu Lv [a,b,c], Hongyuan Li [a,b,c,*]

[a] State Key Laboratory for Turbulence and Complex Systems, Department of Mechanics and Engineering Science, BIC-ESAT, College of Engineering, Peking University, Beijing, 100871, China
[b] Nanchang Innovation Institute of Peking University, Nanchang, 330096, China
[c] Joint Laboratory of Marine Hydrodynamics and Ocean Engineering, Laoshan Laboratory, Qingdao, 266237, China
[d] Key Laboratory for Mechanics in Fluid Solid Coupling Systems, Institute of Mechanics, Chinese Academy of Sciences, Beijing, 100190, China
[e] School of Engineering Science, University of the Chinese Academy of Sciences, Beijing, 100049, China

ARTICLE INFO

ABSTRACT

Cross-domain vehicle (CDV) is able to navigate in different domains, having a wide range of applications in military and civil fields. However, most of the existing CDVs have limited size and payload, which restrict their development in complex oceanic conditions. In this paper, we analyze the cross-domain process and propose a novel CDV, which is characterized by two sets of hydrofoils and foldable airfoil to ensure better hydrodynamic and aerodynamic performance. Through theoretical modeling and numerical simulations, the functions of the feature structures along with their mechanisms are thoroughly investigated. The hydrofoils allow the CDV to glide and take off rapidly, and serve as a buffer zone for impact reduction during surface landing. Meanwhile, the foldable tandem airfoils make significant contributions to the flight stability and efficiency of the CDV. Furthermore, the prototype equipped with the control system is fabricated and experimented, verifying the feasibility and reliability of our design. The cross-domain method and structural design proposed in this paper will provide useful guidance to the future development of novel CDVs.

1. Introduction

Nowadays, various kinds of marine autonomous systems have been developed, including unmanned aerial vehicle (UAV) (Barbarino et al., 2011), unmanned ship vehicle (USV) (Lou et al., 2022; Ozturk et al., 2022) and autonomous underwater vehicle (AUV) (Cui, 2018), and are revolutionizing our capacity of marine exploration, monitoring, and exploitation. In the defense, industry and policy sectors, they have a wide range of applications such as multidomain communication, anti-mine operations and data acquisition, whereas their civil and academic use is getting increasing attention, mainly involving deep-water exploration, sunken salvage and marine data collection. However, most of current autonomous systems can only work in a single domain, aerially or underwater, which greatly limits the range of operations. In order to improve the spatial resolutions of a broad spectrum of possible marine activities, efforts were made to develop a collaborative team of heterogeneous vehicles, but it is difficult and costly to integrate heterogeneous vehicles into one compatible system (Ross et al., 2019).

Striving to combine the advantages of UAV and AUV(Yao et al., 2019) and enable cross-domain operations both aerially or underwater, hybrid aerial underwater vehicles (HAUV) have been developed rapidly in recent years (Zeng et al., 2022; Lyu et al., 2022; Wynn et al., 2014).

The concept of water-air fusion was first proposed before World War II, and the flying submarines designed by the Soviet LPL project were a product of this concept (FLITETEST, 2018). In accordance with the structural characteristics of the vehicles, HAUVs can be roughly classified into three types: rotary-wing, bionic and fixed-wing vehicles. "Naviator" (Ravell et al., 2018; Maia et al., 2017; Villegas et al., 2017; Mercado et al., 2017) realized the conversion from air to water domain through the dual-layer structure of two groups of quadrotors. "HyDrone" (Drews et al., 2014; Horn et al., 2020) also adopted the dual-layer rotors, which were divided into air and water groups. It has been shown that multi-rotor structure improves the performance of underwater navigation. Tan et al. (Tan and Chen, 2019, 2020) designed an aerial-aquatic vehicle with a variant quadrotor and remote operated vehicle (ROV) thrusters, making it possible to work underwater. The rotary-wing

HAUVs are characterized by good maneuverability, but are difficult for engineering use due to its small size, low energy efficiency and limited payloads.

Amy Gao et al. (Gao and Techet, 2011) took inspiration from flying fish and invented an aerial-underwater bionic robot. Robert Siddall (Siddall et al., 2017) then proposed a unique concept of AquaMAV. Imitating the diving characteristics of the booby, they designed a foldable swept wing structure to enable the AquaMAV to "jump out of the water". The bionic HAUV usually has high flexibility, while the control system is rather complicated and the underlying mechanisms largely remains elusive. At present, it is still in the stage of laboratory research and needs further investigation before engineering application.

"Pelican" (Weisshaar, 2013), developed by Lockheed Martin of the United States, is a water-air multi-function UAV with foldable airfoils in the shape of seagull wings, and can be launched from underwater into the air through submarines. "SailMAV" (Zufferey et al., 2019) is a sailboat-like vehicle with three-section foldable airfoils to deal with distinctive functional requirements during sailing and take-off. Moreover, Joseph Moore (Moore et al., 2018) proposed a triangular-wing aerial underwater vehicle with the ability of oblique water exit and autonomous navigation. Hu(Hu et al., 2017) put forward a deformable UAV and established a feasible hydrodynamic/aerodynamic model for its water exit process. William Stewart (Stewart et al., 2018, 2020; Weisler et al., 2018) designed a vertical take-off HAUV through the large airfoils used for passive immersion and drainage. Wei (Wei et al., 2022) designed and tested a fixed-airfoil unmanned aerial underwater vehicle (UAUV), which combined inertia and traction thrusters for cross-domain tasks and allowed take-off at a large pitch angle. In general, high efficiency, excellent endurance and relatively simple control system endue the fixed-wing HAUVs with tremendous potential in practical multidomain operations. In addition to experimental methods, numerical simulation is also an important method to study cross-domain processes (Jia et al., 2022). Duan (Duan et al., 2018) completed the take-off simulation of a large seaplane using an improved two-phase flow solver from OpenFOAM. Zhou (Zhou et al., 2023) studied the influence of different coasting speeds on the motion response and vertical overload of a multi-domain vehicle based on the finite difference method. The conditions under which jumping motion occurs were also analyzed to improve the cross-domain stability of the vehicle.

To sum up, in the existing models and studies, following deficiencies have been revealed. The rotor-driven model will increase extra mass of the vehicle and reduce operational efficiency. Meanwhile, the bionic approach of leaping out of the water requires a complex control system and is only suitable for small vehicles. In this paper, we propose a CDV called "QianXiang II", which can take off from water surface through gliding. "QianXiang II" is characterized by two sets of hydrofoils and foldable airfoil. Through numerical simulations and experiments, the functions of the feature structures along with the mechanisms are thoroughly investigated. The results indicate that "QianXiang II" has a larger payload, higher cross-domain efficiency and lower landing impact compared with other aerial underwater vehicles.

The article is organized as follows. In Section 2, the overall design of the CDV is introduced, and the dynamic model of the cross-domain process is established. In Section 3, the hydrodynamic characteristics of the CDV during glide-off and landing are simulated, and the performance of the CDV under different circumstances is investigated. In Section 4, with the control system established, the prototype is fabricated and experimented. Finally, Section 5 summarizes and discusses the results of our research.

2. Overview of cross-domain motion

CDVs combine the advantages of AUVs and UAVs, integrating high-speed surface navigation mode as USV and air flight mode as AUV. The cross-domain process we designed is shown in Fig. 1. In the process, the CDV undergoes various stages in sequence involving low-speed navigating, high-speed navigating, surface take-off, air flight and surface landing. The CDV initially rests on the water surface, and the airfoils are folded. During the cross-domain operation, the jet propeller at the tail of the CDV is first activated for surface acceleration. Then the airfoils are unfolded, the head propeller starts, and the CDV sails at high speed on water surface. As speed increases to the threshold, the overall lift is larger than the gravity, and the CDV will take off. During the CDV's landing, the speed gradually decreases, and the airfoils are retracted and the vehicle eventually switches to surface-sailing mode.

2.1. Overall design of CDV

The overall geometry of the CDV is shown in Fig. 2(a). The main body is approximately a rotating body. An air propeller is installed on the head and a vector water jet propeller on the tail of the CDV. For the surface take-off, two sets of foldable airfoils are placed on the back of the CDV. Two sets of T-shaped hydrofoils are placed on the belly of the CDV. The attack angle during take-off is controlled by the height difference between the hydrofoils. A hydro fin is also designed on the side of the rear hydrofoil, which can increase the stability of surface navigating, as shown in Fig. 2(d).

The detailed configuration of the CDV is illustrated in Fig. 2(d). The total length of CDV is 2.0 m and the spread length of the front airfoil is 2.4 m. The CDV is made of aviation wood, and many ring frames are
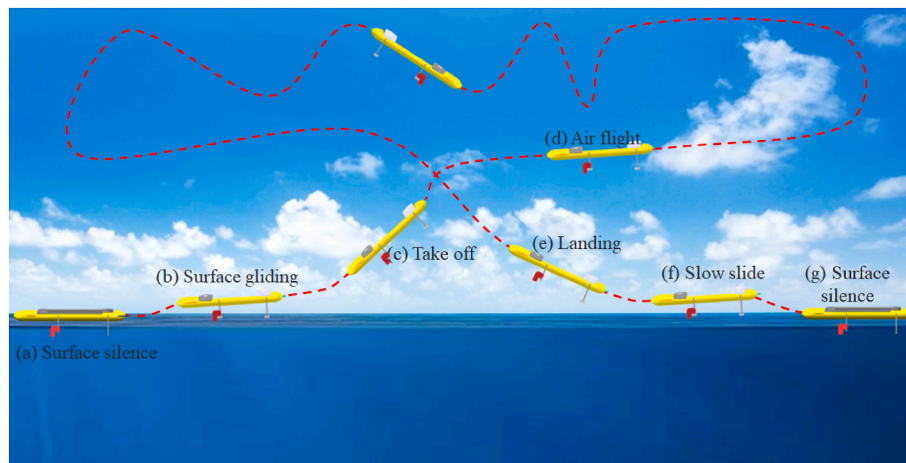

Fig. 1. The cross-domain process of CDV. The CDV rests on surface, then it glides off and execute flight mission before returning to the surface. Dotted lines indicate trajectory of the vehicle.
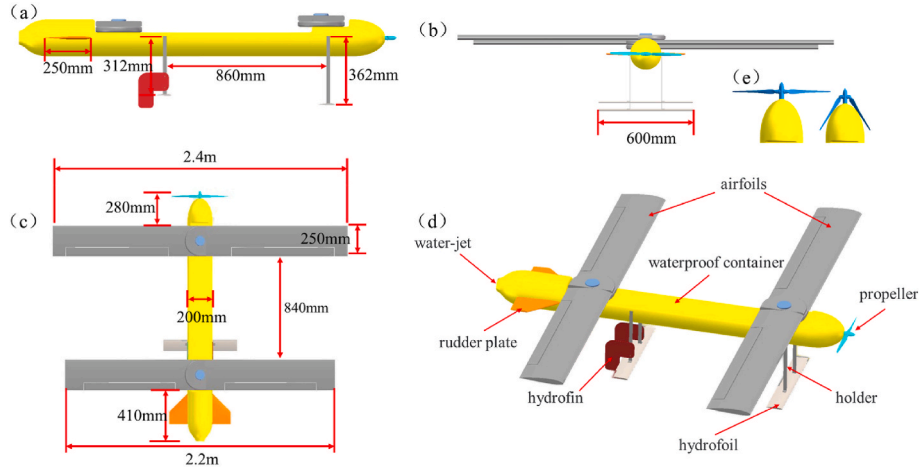
Fig. 2. 3D view of the CDV. (a) side view; (b) elevation view; (c) overhead view; (d) isometric view; (e) foldable propeller.

installed inside the fuselage to improve the structural strength. The CDV below the waterline is made watertight, and the fuselage is divided into several independent compartments, which can further increase the reliability of waterproofing.

The tandem airfoils serve as the main source of lift. The distance between the front and rear airfoils is 840 mm. The chord and span of the airfoils are mainly determined by the total weight of the CDV. With NACA2412 selected as the airfoil, and considering the size and weight of the CDV, the chord length of the airfoils is 250 mm, and the length of front and rear airfoils is 2.4 m and 2.1 m respectively.

Two sets of hydrofoils can not only improve the CDV's speed on surface for rapid gliding and take-off but also reduce the impact on the CDV's fuselage when it lands on the surface. The chord length and the span length of the hydrofoils are 60 mm and 900 mm. The distance between two sets of hydrofoils is 860 mm, and the front and rear hydrofoil have the height of 362 mm and 312 mm respectively. The height difference between the two sets of hydrofoils allows the bow of the CDV to rise. The angle of attack between the CDV and the water surface is 3.3°, which provides a favorable attitude for the CDV to take off. According to the vertical and horizontal distance of the hydrofoils, it can be estimated that the pitch angle of the CDV is about 3.3° when it travels at high speed on the water surface. In practice, since the mass center of the CDV is between the front and rear hydrofoil, the submerged volume of the front and rear hydrofoil is not equal, so the actual take-off angle will be slightly greater than 3.3°.

The main power of the CDV is provided through air propeller. According to the overall aerodynamic design of the CDV and the requirements of the task, we determined the parameters of the air propeller, such as the radius, navigational speed and the number of blades. The air propeller is designed to be foldable, and is folded when sailing at low speed on the water, as shown in Fig. 2(e). When the CDV switches to cross-domain mode, the air propeller opens and rotates at a predetermined speed. It should be noted that the air propeller does not touch the water, otherwise it may cause trajectory deflection and damage to the structure.

2.2. Dynamic model of cross-domain process

In theoretical analysis of cross-domain process, the simplified model is specified in Fig. 4(b), the global coordinate system based on the horizontal plane is defined as x, y and z axes. Local coordinate system with the mass center of the CDV is also defined, i.e., i, j and k axes. These coordinate systems are used to establish the longitudinal dynamic equations of the CDV. The motion of the CDV can be determined by six degrees of freedom, namely $r = [x, y, z]^T$ and $\Omega = [\delta, \vartheta, \varphi]^T$. The former is the position vector in the global coordinate system, and the latter is the attitude angle vector in the global coordinate system. The global coordinate system and local coordinate system can be related by Coordinate Transformations.

As shown in Fig. 3, the cross-domain process of CDV can be divided into three modes: low speed on water surface, high speed on water surface and air flight, and it is necessary to establish different dynamic models for the three modes. At low speed, the forces acting on the CDV include gravity, buoyancy, thruster thrust, resistance and lift of hydrofoil. In this mode, the nonlinear longitudinal dynamic model of the CDV can be expressed as equation (1).

$$
\begin{aligned}
m_i \dot{U}_x &= P_W - F_R - F_{L1}\,sin\,\alpha - F_{L2}\,sin\,\alpha \\
m_i \dot{U}_z &= G - F_B - F_{L1}\,cos\,\alpha - F_{L2}\,cos\,\alpha \\
L_y \ddot{\theta} &= M_{L2} - M_{L1}
\end{aligned}
\tag{1}
$$

With the unfolding of the airfoils and the increase of the speed, the pitch angle of the CDV will change. This results in a change in the relative position between the buoyancy center and the gravity center of the CDV. In this mode, the CDV is mainly subjected to gravity, buoyancy, pulling force of the air propeller, resistance and lift, as shown in Fig. 4 (b). The lift is mainly provided by the hydrofoils and the airfoils. The nonlinear longitudinal dynamic model of the CDV can be further expressed as equation (2). It should be noted that added mass of water will reduce with the decrease of the CDV's wet surface area. The resistance of the CDV in the air is ignorable compared with the resistance in the water. In the theoretical analysis, we assume that the added mass is positively related to the draft, then the mass change of the CDV during the mode of high-speed sailing can be expressed as equation (3).

$$
\begin{aligned}
m_i \dot{U}_x &= P_A\,cos\,\theta - (F_{L1} + F_{L2})sin(\alpha + \theta) - (D_1 + D_2)sin(\gamma + \theta) - (T_1 + T_2)sin(\beta + \theta) \\
m_i \dot{U}_z &= F_B + P_A\,sin\,\theta + (F_{L1} + F_{L2})cos(\alpha + \theta) - (D_1 + D_2)cos(\gamma + \theta) - (T_1 + T_2)cos(\beta + \theta) \\
L_y \ddot{\theta} &= M_B + M_{PA} + M_{L2} - M_{L1} + M_{D2} - M_{D1} + M_{T2} - M_{T1}
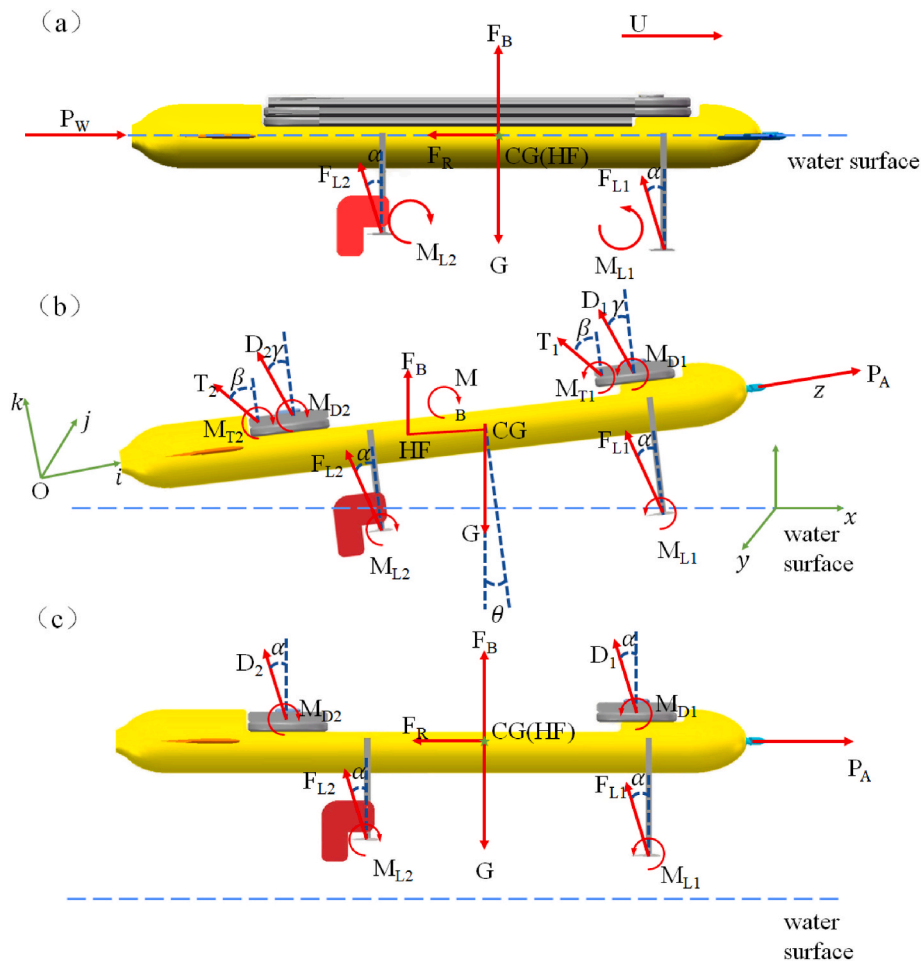\end{aligned}
\tag{2}
$$

Fig. 3. Schematic of forces on the CDV under different modes. (a) Low speed sailing; (b) high speed sailing; (c) air flight.
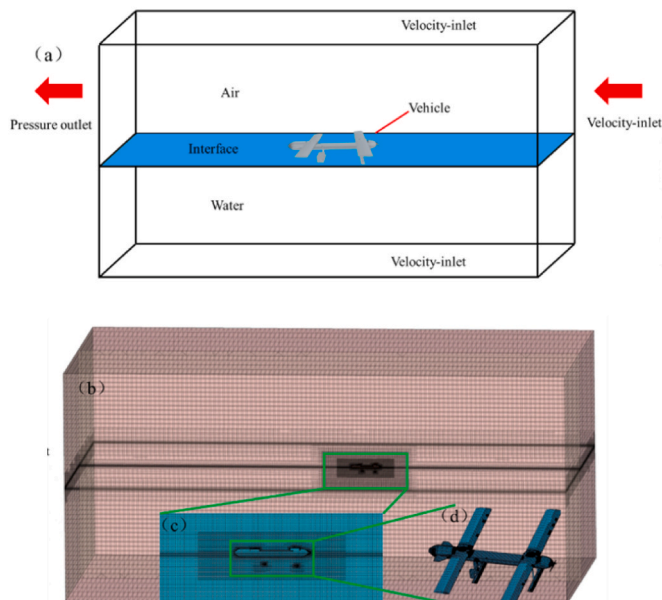

Fig. 4. Schematic of numerical model. (a) Fluid computing domain; (b) global computing grid; (c) overset grid; (d) structural surface grid.

$$m_i = m + \frac{d}{H}\lambda_i \sin\theta \tag{3}$$

When the CDV is completely out of the water, it flies like a fixed wing UAV. During the mode of air flight, the center of buoyancy and the center of gravity are on the same vertical level. At this time, the force on the vehicle is shown in Fig. 3(c). Since the viscosity coefficient of air is far less than that of water, the influence of the added mass of air on the CDV can be ignored during the mode of air flight. The nonlinear longitudinal dynamic model of the CDV can be expressed as equation (4).

$$
\begin{aligned}
m\dot{U}_x &= P_A - F_R - (F_{L1} + F_{L2} + D_1 + D_2)\sin\alpha \\
m\dot{U}_z &= G - F_B - (F_{L1} + F_{L2} + D_1 + D_2)\cos\alpha \\
L_y\ddot{\theta} &= M_{L2} - M_{L1} + M_{D2} - M_{D1}
\end{aligned}
\tag{4}
$$

The variable used in this paper are specified in appendix.

In our study, dynamic models under different states are the theoretical basis for CDV cross-domain motion simulation. Meanwhile, many design parameters are estimated by the model, such as the level flight speed and the payload.

3. Simulation and analysis of cross-domain process

3.1. Numerical calculation model

The attitude change during gliding-off and landing is an important factor in determining the rationality of CDV design. Through numerical simulations, we analyze the dynamic characteristics of the CDV. Taking

the navigation resistance as an index, we tested the effects of grid size and time step on the accuracy, efficiency and stability of numerical simulation.

Taking the surface navigation state when the airfoil is unfolded as an example, the hydrodynamic performance of the CDV is simulated. The calculation domain is shown in Fig. 4, the right, upper and lower boundary are defined as the velocity inlet. The left boundary is set as the pressure outlet, and the other boundaries are defined as the symmetry plane. VOF (Volume of Fluid) (Zhou et al., 2022; He et al., 2021) is selected as the multiphase model for the calculation model. This method can effectively reconstruct the interface that does not blend with each other. In the calculation process, we use second-order upwind scheme (convective term), second-order implicit scheme (time discretization) and the SIMPLE algorithm (pressure-velocity coupling term).

For the CDV with complex geometry, distortion of the grid will easily occur with a large grid scale, resulting in a large deviation of simulation from actual situations. However, with a small grid scale, the number of grids will rise dramatically as well as the simulation time. Therefore, it is imperative to select an appropriate grid size, which simultaneously meets the requirements of calculation accuracy and calculation cost.

Taking the model at the speed of 1 m/s as an example, we set the surface mesh size of the vehicle as 2 mm, 4 mm, 7 mm, 10 mm, 20 mm and 40 mm, respectively. The number of grids at different grid scales is shown in Table 1.

When the mesh size is 2 mm, the mesh is dense enough to easily increase the error if we continue to densify the grid, and with the size of 40 mm, the mesh is coarse enough to cause distortion on the surface while further increasing mesh size. The results of CDV's friction resistance under different surface grid sizes are shown in Table 2, where the theoretical values are calculated using the ITTC conference empirical formula (Ravenna et al., 2022).

As can be seen from Table 2, with the increase of the mesh size of the CDV's surface, the deviation of the simulation result of friction resistance from the theoretical value gradually increases. When the grid size is less than 4 mm, the friction resistance calculation results do not change significantly. Considering the calculation cost, 4 mm is finally selected as the surface grid size of the CDV. Meanwhile, the fluid domain mesh is shown in Fig. 5(b).

The time step is also an important factor that affects the convergence speed and accuracy of simulation for the problem of turbulence with a free surface. For different numerical models, there exists a correspondingly optimal time step in theory considering the accuracy and efficiency of simulation. Therefore, in this work, the numerical model is calculated with different time steps set as 0.0001s, 0.0005s, 0.001s, 0.005s, 0.01s and 0.05s. The calculation conditions and boundary conditions are shown in Fig. 4(a), and the resistance is again taken as the comparative parameter. The results are shown in Table 3. Fig. 5(a) shows the convergence curve of the numerical model with different time steps. Fig. 6(b) shows the error curve of resistance with different time steps. It can be seen from these results that when the time step is greater than 0.01s or less than 0.0005s, there is a large deviation of the numerical results from theoretical ones, and the maximum error can reach 20.5%. To summarize, when the time step is set to 0.001s, the error between numerical and theoretical results, as well as the convergence time is relatively small.

Table 1
Grid size and number settings.

Grid size/mm	Grid number/10^4	Grid size/mm	Grid number/10^4
2	1563.2	10	373.4
4	924.1	20	186.9
7	596.5	40	92.1

Table 2
Calculation results of different grid sizes.

Grid size/mm	Theoretical result/N	Simulation result/N	Percentage error/%
2	1.532	1.511	1.9
4	1.532	1.507	2.3
7	1.532	1.494	3.6
10	1.532	1.485	4.5
20	1.532	1.473	5.7
40	1.532	1.461	6.9

3.2. Gliding off from water surface

The CDV designed in this study has two modes on the water surface, but the CDV can only navigate at low speed on water surface when the airfoils are folded, which is similar to the traditional ship. Therefore, in this section, we analyze the CDV gliding off from the water surface.

Complex and narrow region like the connecting part between airfoils and fuselage, can cause misconvergence and a great waste of time, but have little impact on the overall performance. Thus, these regions are simplified, and the simplified model is shown in Fig. 4(d).

Firstly, we estimate the aerodynamic characteristics of the CDV through lift surface method. The lift force of the vehicle can be expressed by equation (5).

$$L = \frac{1}{2}\rho v^2 S C_l \qquad (5)$$

The CDV has a mass of 7.5 kg and a wing area of about 1.2 m². Fig. 6 shows the airfoils selected in this work and lift-drag ratio curves of them. It can be seen from the results that when the attack angle is 5°, consistent with the installation angle, the lift-drag ratio reaches the maximum. The CDV is designed to take off at 3.3°, so the total attack angle of the airfoil during take-off is 8.5°. At this angle, the lift coefficient of airfoils is 1.2. By substituting these parameters into formula 5, the take-off speed of the CDV can be calculated to be about 9.3 m/s.

Firstly, we estimate the aerodynamic characteristics of the CDV through lift surface method (see Fig. 7). Given the airfoil area and initial installation angle of wings, we can estimate the take-off speed to be about 9.3 m/s. Fig. 6 shows the airfoils selected in this work and lift-drag ratio curves of them. It can be seen from the results that when the attack angle is 5°, consistent with the installation angle, the lift-drag ratio reaches the maximum.

We divide gliding off of the CDV into three stages, namely low-speed navigation, high-speed navigation and take-off. Correspondingly, six groups of different flow velocities are discussed. Fig. 8(a) shows the navigation resistance of CDV at different speeds. Fig. 8(b) shows the change of the height of mass center at different speeds. Fig. 8(c) shows the change of pitch angle at different speeds.

It can be seen from the results that with the increase of speed, the overall resistance of the CDV climbs up and then declines. This can be attributed to the acceleration of CDV and then losing contact with water surface when lift dominates. By further comparing the heaving of the CDV under different speeds, it shows a critical speed between 8m/s-10 m/s, i.e., take-off speed. This result is consistent with the critical speed obtained through theoretical analysis.

Furthermore, when the speed is 6 m/s, the resistance of the CDV has drastic fluctuations, and the gap between peak and valley can even reach 15 N. Through further analysis, it is found that part of the front hydrofoil is above the water surface, but soon falls back due to the lack of lift. This reciprocating variation results in dramatic fluctuations in drag at that speed. With respect to mass center and the pitching of the CDV at different speeds, it is shown that as speed increases, the pitching angle of the vehicle gradually approaches 3.7° and then glides off from water, which is consistent with the designed take-off angle. This special state is the transition state of CDV from low-speed to high-speed and stable navigation. Through our improved design of hydrofoil, we can reduce
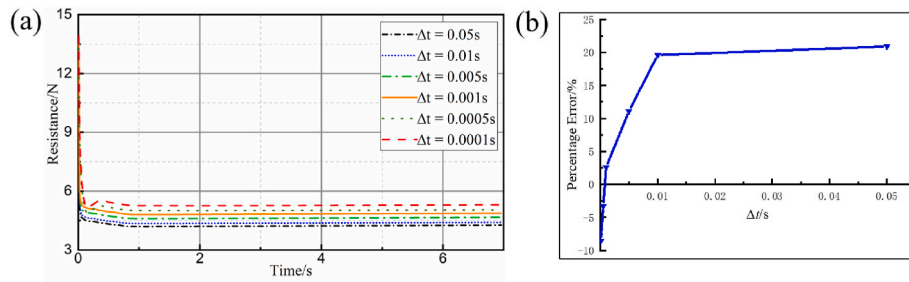
Fig. 5. Convergence of grid. (a) The relationship between different time steps and resistance; (b) relative errors with different time steps.

Table 3
Resistance comparison at different time steps.

Time step/s	Theoretical result/N	Simulation result/N	Percentage error/%
0.0001	1.532	1.662	8.5
0.0005	1.532	1.581	3.2
0.001	1.532	1.493	−2.5
0.005	1.532	1.368	−10.7
0.01	1.532	1.238	−19.1
0.05	1.532	1.217	−20.5

the influence of the transition state on the stability of CDV. This will be the focus of our next research on CDV optimization.

With respect to mass center and the pitching of the CDV at different speeds, it is shown that as speed increases, the pitching angle of the vehicle gradually approaches 3.7° and then glides off from water, which is slightly larger than the initial design angle of 3.3°. This error is caused by the difference in the volume of the front and rear hydrofoil immersed in water, which is consistent with the design prediction. Fig. 9 shows the lift of various components at different flow velocities. It can be seen from the results that during low-speed navigation, the lift of the hydrofoil is obviously higher than that of the airfoil, and the front hydrofoil accounts for the largest proportion of total lift. During acceleration, the angle of attack gradually approaches to the set value, and the lift of the airfoil dramatically increases. When the navigation speed of the CDV exceeds the critical speed, the lift provided by the hydrofoil drops sharply due to leaving the water surface. At this time, the airfoil becomes the main source of lift, and the CDV switches into air flight mode. During the whole cross-domain process, the total lift of the CDV is approximately equivalent to the gravity.

In order to verify the lift-enhancement effects of hydrofoil during take-off, for comparison, we establish another numerical model without hydrofoil on the water surface at of 8 m/s. The results are shown in Fig. 10. It can be seen that compared with that equipped with hydrofoils, the navigation resistance and pitch angle, along with amplitude of their oscillation significantly decline. Specifically, according to the simulation results, the hydrofoil structure can reduce the navigation resistance of the aircraft by about 32% and the pitch angle by about 43%.
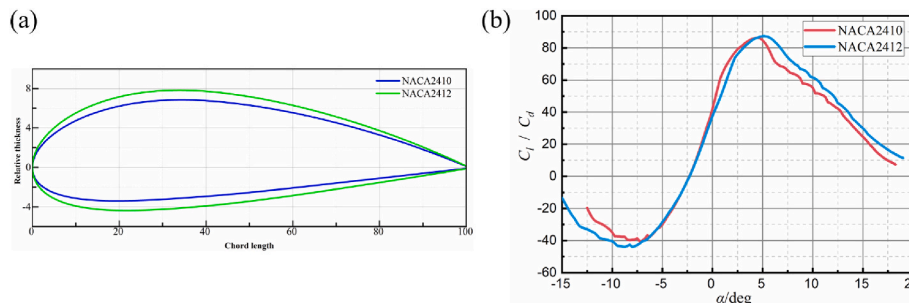
3.3. Air flight

This section mainly focuses on the aerodynamic performance of the CDV, and discusses the coupling effect between the tandem airfoils. We select NACA2410 as the airfoil , of which the lift-drag characteristics have been given in Fig. 6. To make lift-drag ratio of the airfoil reach its maximum, the installation angle of wings is preliminarily set as 5°.

As to the entire vehicle, the relationship between lift, drag and level speed is presented in Fig. 11(a). The balance of weight and aerodynamic lift during level flight requires the cruising speed of at least 15 m/s. Fig. 11(b) illustrates the lift-drag ratio of the CDV and wings at different attack angles, indicating that the lift-drag ratio peaks at about 0°, and stall occurs at around 15°.

The pressure distribution on the surface of the CDV is shown in Fig. 12(a and b), and the air velocity in Fig. 12(c and d). As can be seen, the pressure is mainly concentrated on the fuselage head and the leading edge of airfoils. By further comparing the pressure distribution on different airfoils, it is found that due to the existence of the front wings,
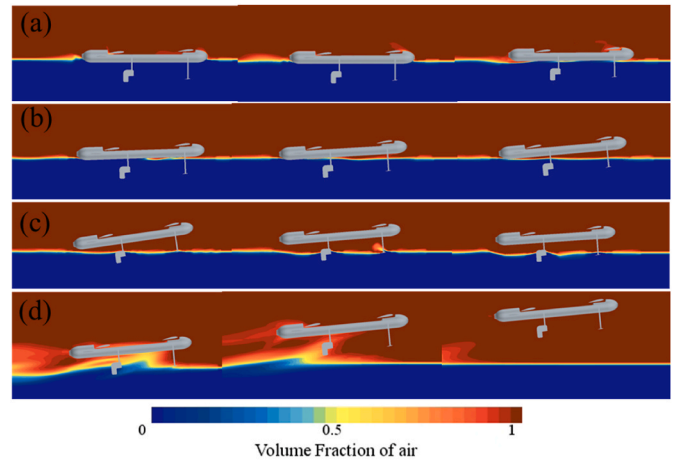

Fig. 7. Simulation results of cross-domain process. (a) Navigation on water at low speed; (b) acceleration; (c) navigation at high speed; (d) glide-off.

Fig. 6. Schematic of airfoil parameters. (a) Airfoil shape parameters; (b) lift-drag ratio of airfoil, C_f stands for the lift coefficient, C_d stands for the drag coefficient.
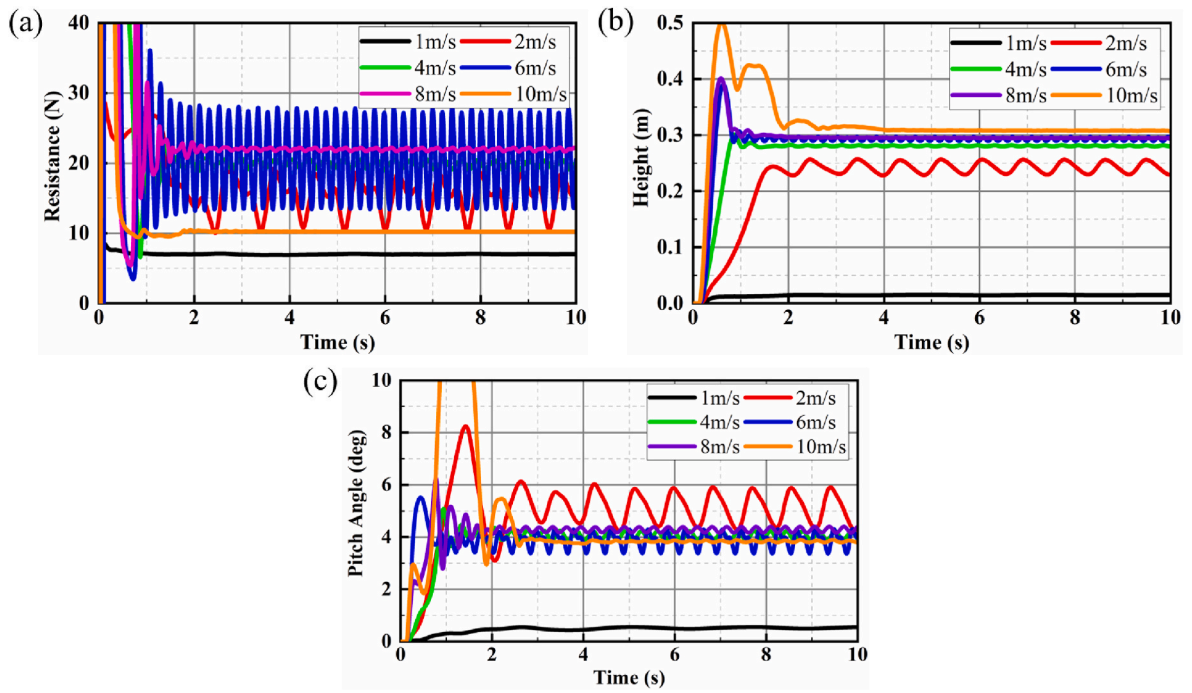
Fig. 8. Motion state of the CDV at different speeds. (a) Resistance at different speeds; (b) height of mass center at different speeds; (c) pitch angle at different speeds.
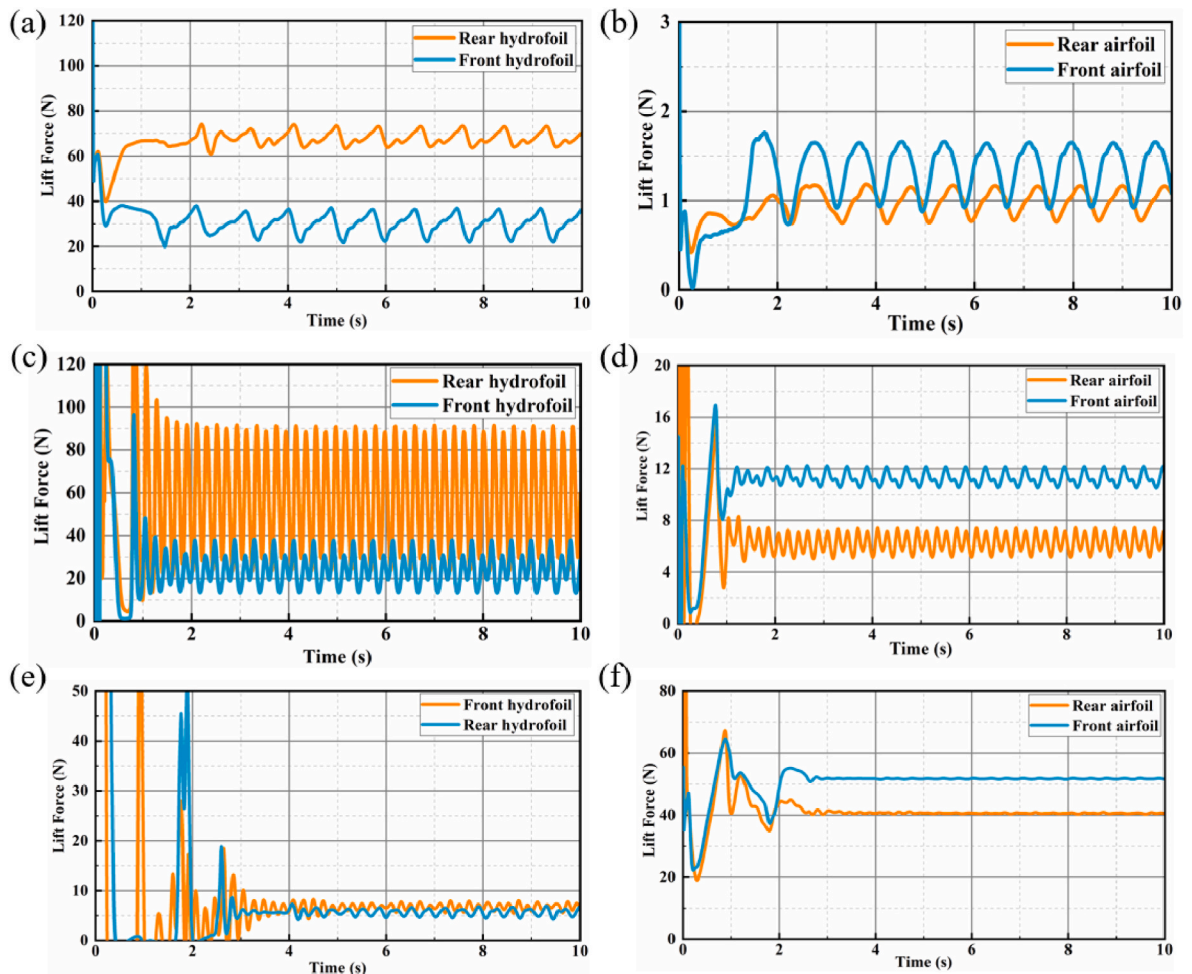

Fig. 9. Lift of hydrofoil and airfoil at different speeds. (a, b) Speed = 2 m/s; (c, d) speed = 6 m/s; (e, f) speed = 10 m/s.
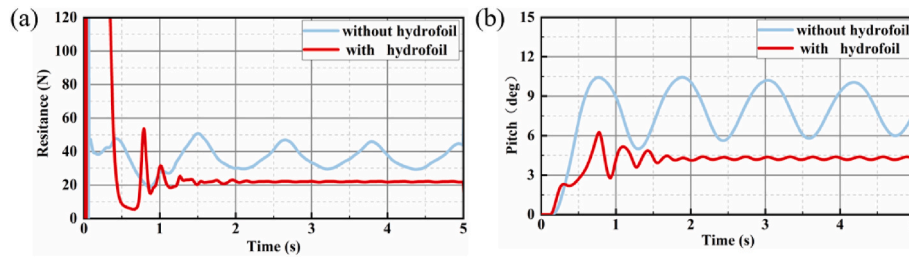
Fig. 10. The influence of hydrofoil on the motion state of the CDV. (a) Effect of hydrofoil on resistance; (b) effect of hydrofoil on pitch angle.
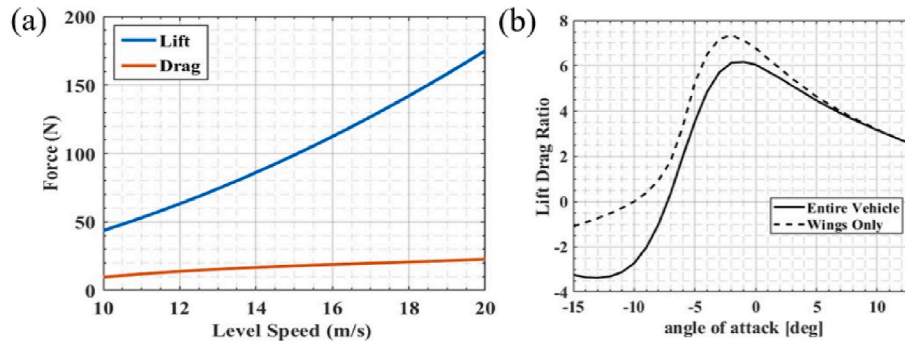

Fig. 11. The relationship between lift and drag in the air. (a) Lift and drag at different speeds; (b) lift-drag ratio at different angles of attack.

the leading-edge velocity of the rear airfoil is reduced, which leads to higher pressure on the surface of the rear wings. Furthermore, Fig. 12(e) shows the vorticity distribution of the CDV at the angle of attack of 7°. Various types of vortices (Park, 2015) can be clearly observed, including tip, leading-edge and trailing vortices. Similarly, the vorticity shows concentration on leading-edge on front wings rather than the rear ones, which further proves a significant interference effect of front airfoil to the aerodynamic performance of rear airfoil. The quantitative description of these effects can be one of the important contents of future research.

3.4. Surface landing

In this section, the whole process of surface landing of CDV is numerically simulated by overlapping mesh (Guo et al., 2021). As shown in Fig. 13, the numerical results show the variation of the vehicle's horizontal velocity, pitch angle, height of the gravity center, vertical velocity, and overload. Overload is a dimensionless parameter, which are defined as follows,

$$\begin{cases} F_x = \dfrac{f_x}{mg} \\[2mm] F_y = \dfrac{f_y}{mg} + 1 \end{cases} \tag{6}$$

where F_x is the horizontal overload suffered by the CDV, f_x is the horizontal force on the CDV, F_y is the vertical overload of the CDV, f_y is the vertical force of the CDV and g is the acceleration of gravity.

The surface landing process of the CDV can be divided into three stages (Yu et al., 2022), including impact stage, sliding stage and floating stage, as shown in Fig. 14. In the impact stage, with certain initial kinetic energy, the CDV suffers a huge impact load due to water entry. The motion of the CDV exhibits remarkable fluctuations, and the pitch angle and vertical velocity have a tendency of drastic oscillation, which may lead to the phenomenon of bouncing. The impact stage is the initial stage of surface landing process with the shortest time. The "valley - peak - valley" of the height of the gravity center is defined as one impact process, and only one impact occurs is simulated. With the

increase of initial horizontal and vertical velocities the number of impacts will also increase.

After impact, the CDV enters the surface sliding stage. During this stage, the CDV does not bounce or pitch violently, but continues to shake slightly. At this time, the energy of vertical motion is gradually consumed, and the energy of horizontal motion is dominant. At this stage, the position of the CDV's gravity center is the primary factor.

With the further reduction of the horizontal velocity, the vertical overload of the CDV tends to be stable, and the hydrostatic buoyancy becomes the main external load on the CDV. Then the CDV switches to a floating stage, the head of the CDV gradually enters the water, and the impact load decreases to a low level.

In order to verify that hydrofoils can effectively improve the stability of landing, we compared the vertical overload of the vehicle fuselage area with and without hydrofoil, and the results are shown in Fig. 13(d). It can be seen that the vertical overload of the fuselage area with hydrofoil is obviously lower than that without hydrofoil. This is because the hydrofoils serve as the buffer zone between the vehicle fuselage and the water surface, reducing the impact load on the CDV fuselage directly from the water.

4. Power electronic system

According to the structure and function characteristics of the CDV, the power electronic system of the vehicle is designed with functional modularization. The power electronic system of the CDV is divided into five subsystems, namely, the power system, the decision system, the communication system, the information sensing system and the motion control system.

The main function of the power system is to supply power to each module. In order to keep the power supply stable, the battery capacity and output voltage are 1000Wh and 25.9 V respectively, and the maximum output current can reach 20 A. The battery voltage can be stabilized at 5 V, 12 V and 24 V output respectively through three groups of voltage regulator modules. Therefore, the power system can meet the requirements of supply voltage for all subsystems. In Fig. 14(a), the power supply of each component is specified in detail (e.g., the steering motor driver is powered at 5 V, and the water jet motor driver is
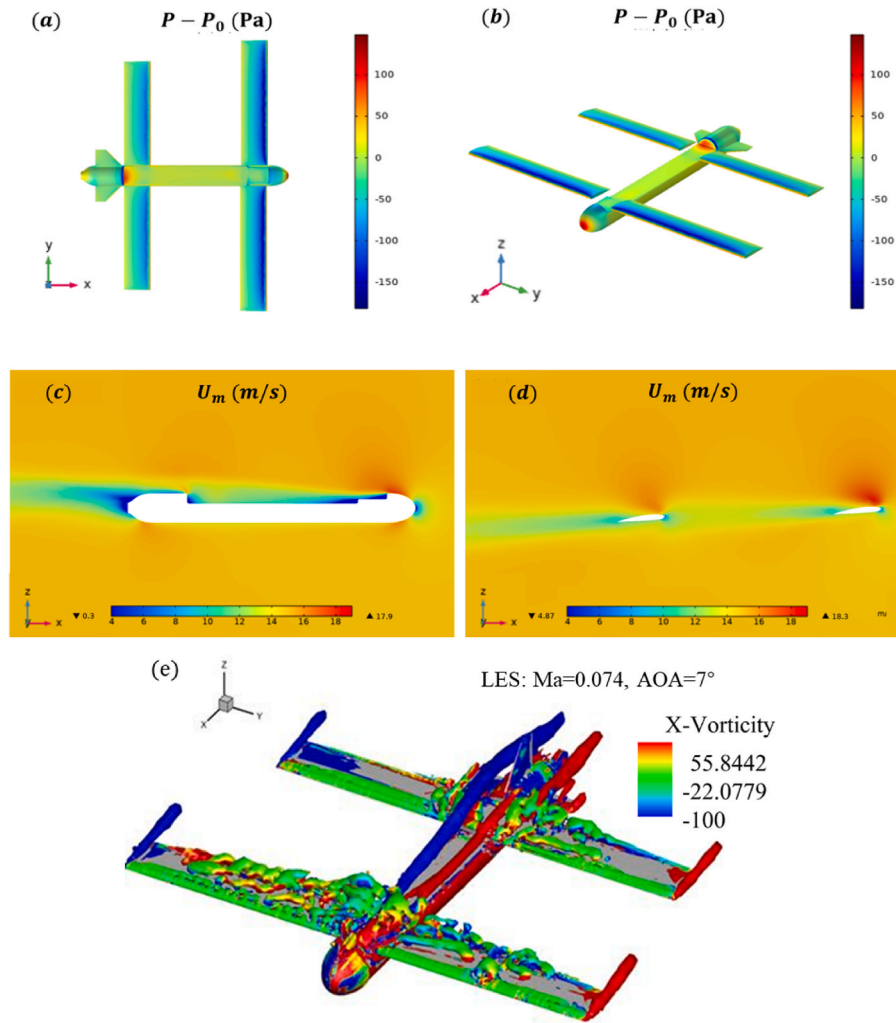
Fig. 12. Numerical simulation results when CDV flies at speed of 15 m/s (a, b) Pressure distribution on the surface of the CDV; (c, d) distribution of air velocity around the CDV; (e) vortex distribution around the CDV, *Ma* stands for Mach number and AOA stands for angle of attack.

powered at 24 V).

The motion control system is mainly used to control the navigation speed and direction of the CDV. In order to make the propulsion of the vehicle more stable, multiple motor drivers and multiple electronic speed controllers (ESC) are used to drive the corresponding motors and rudders. The motion control system also consists of following components: a water jet propeller to provide forward propulsion, a steering gear to adjust the direction on water surface, a propeller motor to provide aerial flight power, two motors to control airfoil folding, and four airfoil ailerons rudders to adjust the direction in air. The micro control unit (MCU) can output multiple pulse width modulation (PWM) signals to the motor drivers and ESC to make the rudders and motors work.

The information sensing system mainly consists of pitot tubes, inertial measurement unit (IMU), BeiDou navigation module and water leakage sensors distributed at the joints of each section of the CDV. Pitot tubes are used to measure the speed of a vehicle in the air (Wen et al., 2020). The attitude and heading angle of the CDV are obtained by the IMU. The above are the key and necessary equipment for the automatic navigation of the CDV in air and on water surface. In addition, the water leakage sensors can effectively detect whether there is water leakage in each section of the CDV and send out timely warning signals.

The main equipment of the communication system consists of 433 MHz radio telemetry module, 2.4 GHz remote control receiver and BeiDou satellite communication module. The main function of 433 MHz radio telemetry module is to communicate with the ground station under limited distance and frequency band, while the BeiDou satellite communication module communicates with ground equipment remotely. The 2.4 GHz remote control receiver is mainly used to receive propulsion control signals in manual mode.

The decision-making system mainly includes a micro control unit (MCU), an SD card for information storage and a battery management system (BMS) for real-time monitoring of battery power. The MCU can receive different equipment information through different signal transmission modes (RS232, RS485), and control the propulsion system through PWM signals.

The ailerons of airfoils and their driving motors are the main mechanism to control the navigation attitude of the CDV. The MCU controls the aileron drive motor to change the aileron angle, thus altering the amount of lift provided by airfoils. By aileron driving motors, the attitude of the CDV can be adjusted during the steering, take-off and landing. Therefore, we design a double-loop cascade feedback control system to precisely control of navigation attitude. The control flow is shown in Fig. 15(a).

In Fig. 15(a), $\varphi_d, \theta_d, \varphi_d$ represent the expected roll angle, yaw angle and pitch angle respectively. p_d, q_d, r_d stand for the expected X, Y and Z angular velocities, and u_p, u_q, u_r represents the controls parameter of angular velocity. The angular and angular accelerations shown in Fig. 15 (a) are obtained by the gyroscope and accelerometer in the IMU. The attitude angle and angular velocity can be calculated and used in close-loop adjustment. The final angular velocity control quantity is
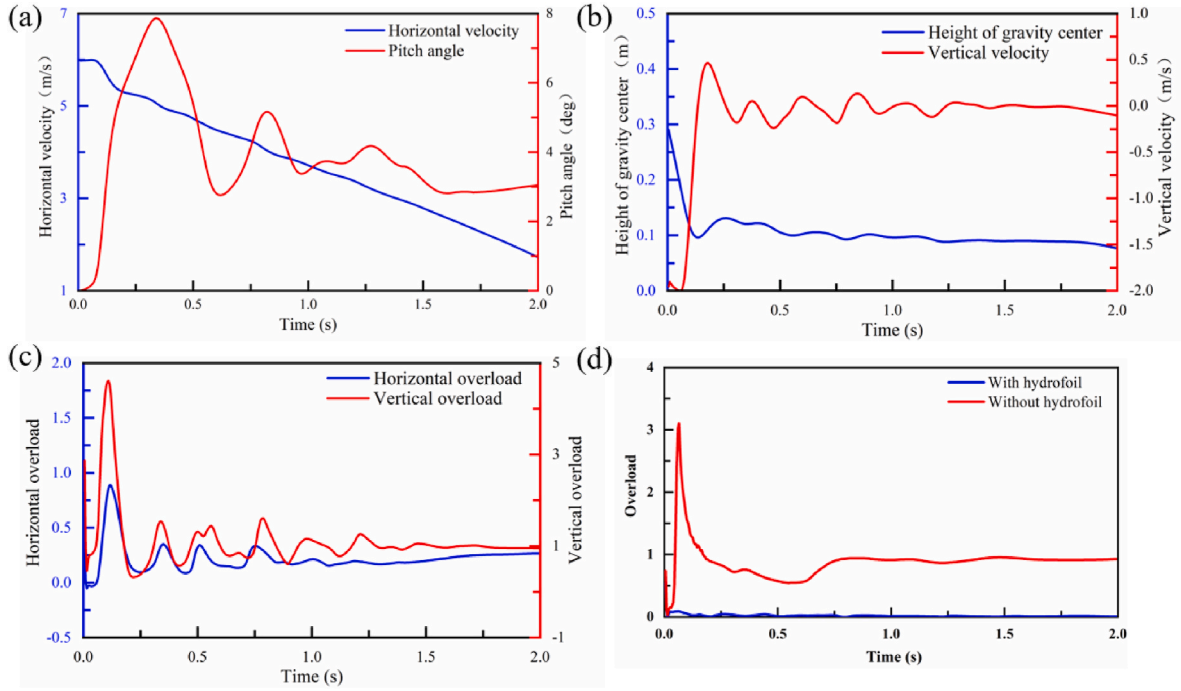
Fig. 13. Landing process of the CDV. (a) Change of horizontal velocity and pitch angle with time; (b) change of height of gravity center and vertical velocity with time; (c) change of vertical and horizontal overload with time; (d) effect of hydrofoil on fuselage overload.

calculated to obtain the control quantity of the four-aileron steering gear. We use the weighted sum of the control quantities of the four-aileron steering gear to represent the control quantity of angular velocity. By obtaining the control quantity of each angular velocity, the actual control quantity of each aileron steering gear u_1, u_2, u_3, u_4 with a certain constraint range ($\{u_i : u_{min} < u_i < u_{max}, i = 1, 2, 3, 4\}$) can be calculated, where u_{min}, u_{max} are the minimum and maximum control quantity of each aileron steering gear, respectively. In order to simplify the complexity of the control system, the front and rear aileron steering gears on the same side have the same control quantities, i.e., $u_1 = u_3$, $u_2 = u_4$. The weighted sum of all the aileron steering gear's control quantities is used to represent each angular velocity control quantity, which can be represented by the following formula:

$$u_p = p_1 u_1 + p_2 u_2 + p_3 u_3 + p_4 u_4$$

$$u_q = q_1 u_1 + q_2 u_2 + q_3 u_3 + q_4 u_4$$

$$u_r = r_1 u_1 + r_2 u_2 + r_3 u_4 + r_4 u_4$$

where, $p_1, p_2, p_3, p_4, q_1, q_2, q_3, q_4, r_1, r_2, r_3 r_4$ are the weight of the control quantity of four-aileron steering gear. The actual control quantity of each aileron steering gear can be obtained by solving the formula above.

The main actuator of CDV includes water jet propeller and air propeller. The speed of CDV can be adjusted by autonomously switching and adjusting the output of the jet and air propeller. The navigation speed is adjusted by the fuzzy controller (Tang et al., 2001) and PID controller (Anderson et al., 1988). The control flow is shown in Fig. 15 (b), where V_d stands for the desired speed, $V = V_d - e$ represents the actual speed, and K_p, K_i, K_d are the three coefficients of proportional differential integration. By fuzzy controller and PID controller, the control system can get the expected output of the propellers.

Further, we combined the vehicle dynamics model (section 2.2) and control flow (Fig. 15) to conduct motion control simulation in this section to verify the effectiveness of the control method and CFD simulation. We use MATLAB and obtain the simulation results of the adaptive fuzzy PID controller, as shown in Fig. 15(c). We also get the self-regulating change process of the adaptive fuzzy PID coefficients, as

shown in Fig. 15(d). Seen from Fig. 15(c), by using an adaptive fuzzy PID controller instead of a traditional controller, the control system has a smaller overshoot and smaller steady-state error, which can achieve better speed tracking control.

5. Cross domain experiments

The prototype was made and tested on the lake, as shown in Fig. 16 (a) The total weight of the CDV is 7.5 kg (exclusive of the payload). We conducted the experiments of water surface acceleration, steering with folding airfoils and most importantly, the cross-domain process of the CDV on the lake. Fig. 16 shows the different stages of the cross-domain process. During this process, the airfoils are unfolded and part of the CDV is immersed in water, as shown in Fig. 16(b). As the air propeller starts, the speed of CDV gradually increases. Then the head of the CDV lifts, forming a large attack angle. When the speed increases to a certain extent, all components of the CDV except the hydrofoils stay above the water surface. The rear hydrofoil produces more broken spray and sputters onto the fuselage of the CDV. When the take-off speed is reached, the front airfoil first leaves the water surface, the attack angle of the CDV increases briefly, and the lift provided by the hydrofoil rises sharply. In a short time, the rear hydrofoil also leaves the water surface. The speed of the CDV further increases, and the motion of the CDV quickly switches to the air flight mode.

The control system of the CDV in air is similar to traditional fixed-wing unmanned vehicle. The air flight state is controlled through the cooperation of air propeller and flap. Fig. 16(d) illustrates the whole process of the water surface landing. As the speed gradually declines, the CDV slowly approaches the water surface. When landing, the hydrofoil first touches the water surface, and then the fuselage touches the water surface after part of the impact is counterbalanced. The process above is a complete cross-domain cycle, and the CDV can repeat the process after attitude adjustment on the water surface. In our experiment, the cross-domain process from water to air was partially controlled by a human pilot. We control the flight path and flight target of the vehicle by remote control, and the speed and attitude of the vehicle can be automatically adjusted by the flight control system.
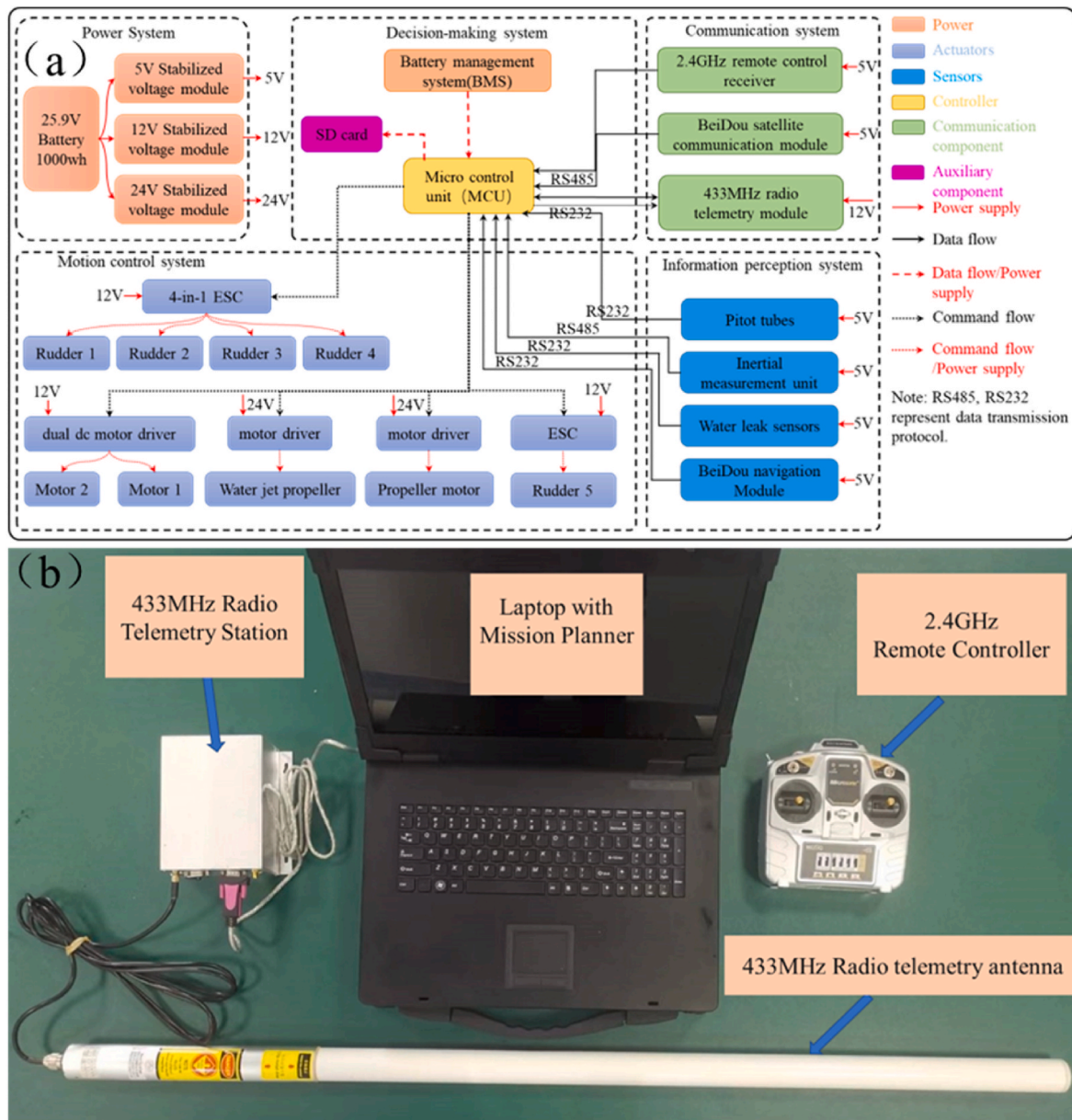
Fig. 14. Schematic of electronic system. (a) Control system and battery system; (b) Ground station equipment.

Fig. 17 (a) and (b) show the velocity and attitude changes of CDV during surface navigation. At 0–6s, the CDV was in the low speed sailing stage on the water surface. At this stage, the CDV is propelled by water jet thrusters and can reach a maximum sailing speed of 3kn. Because the mass center of CDV is close to the bow, there will be a short-buried bow phenomenon during the initial acceleration. With the start of air propeller, the motion attitude of CDV changes dramatically. When the CDV speed is about 2 m/s, the pitch angle undergoes obvious fluctuation. By observing the actual motion state of CDV, it is found that the hydrofoil does not completely out of water at this stage, which is consistent with the result of numerical simulation. When the speed of CDV increases to 4 m/s, the hydrofoil has completely surfaced, and the motion attitude of CDV tends to be stable.

In Fig. 17 (c) , 0–8s is the water surface acceleration process, during which the speed of CDV increases. During the initial acceleration, the pitch angle of CDV showed a rapid fluctuation and gradually stabilized at 4.5°–5.5° with increasing velocity. When the speed of CDV reaches take-off speed, the pitch angle increases rapidly. After some time in the air, the vehicle landed on the water. The final part of Fig. 17 (c) shows

the process of the CDV landing on the water surface. During landing, the bow of the CDV contacts the water surface, followed by rapid oscillation, and finally it stays stationary on the water surface. Due to the rapid reduction of thruster throttle at this stage, the velocity drops rapidly and the attitude of the vehicle changes dramatically. Thus, it is difficult for the CDV to remain stable.

Fig. 17 (d) shows the test results and simulation results of pitch angles at different speeds. The curves of numerical simulation and experimental results have a good agreement on the trend. When CDV is in high-speed sailing state, the error of numerical simulation reaches the minimum, and the relative error is about 4.7%. When the sailing speed of CDV is within the range of 2m/s-7m/s, the error is relatively large. At this stage, the kinetic energy accumulation of CDV is insufficient, and the motion posture is easily affected by the external environment. At the same time, there are slight waves on the water surface of the test site.

Through the experiments, the maximum stable flight speed of CDV in the air is about 18 m/s, the average take-off distance is about 35 m, the air endurance is about 30min, and the turning radius on the water surface is about 4.2 m.
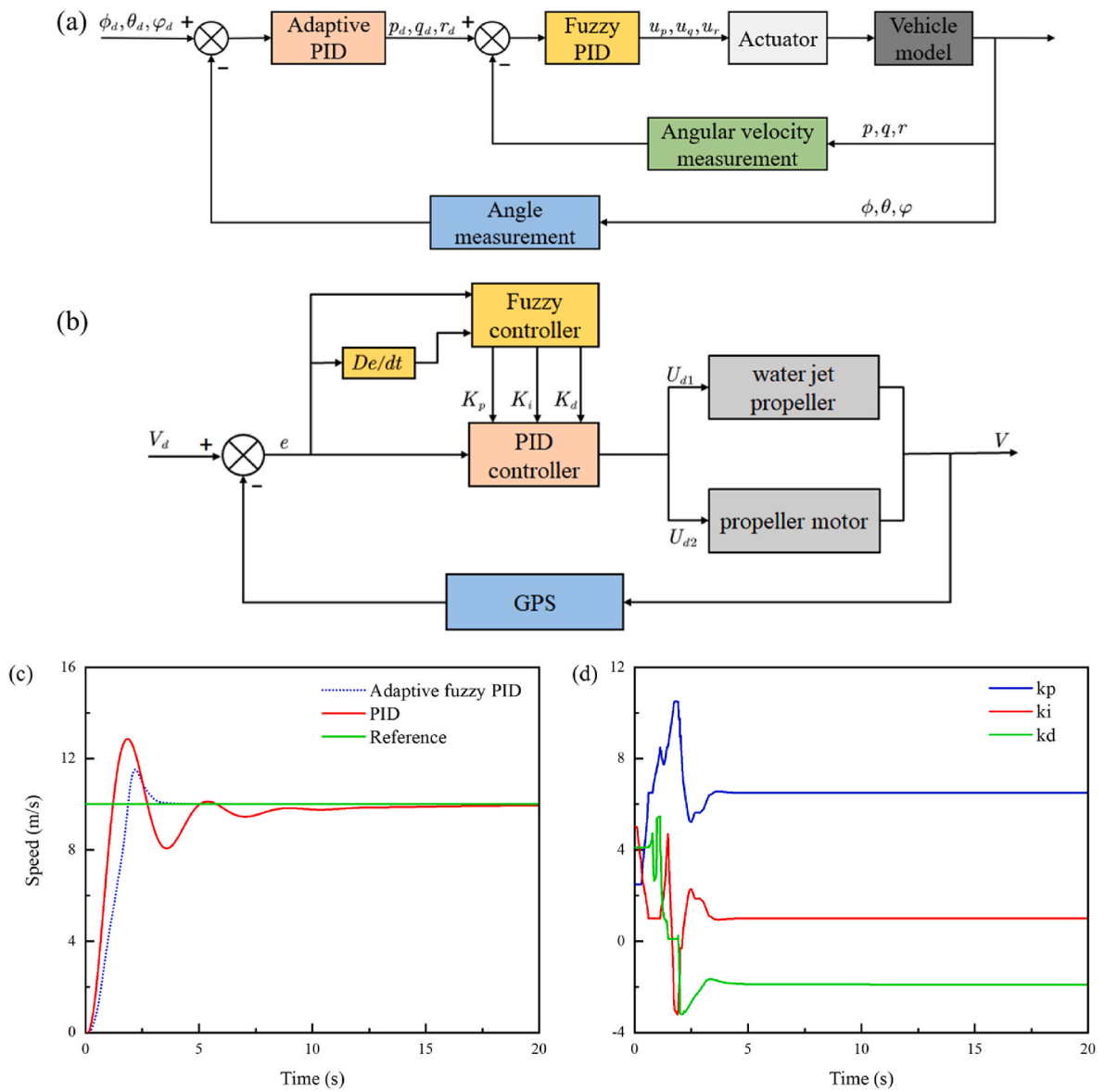
Fig. 15. Schematic of motion control system for CDV. (a) Attitude control flow of CDV; (b) speed control flow of CDV; (c) simulation of adaptive fuzzy PID (Proportion Integration Differentiation) control; (d) adaptive fuzzy PID coefficient self-adjusting change process.

Fig. 16. The cross-domain experiment of CDV on the lake (detailed experimental process see supplementary movie). (a) Surface sailing and steering; (b) high speed sailing and take-off; (c) flying in the air; (d) landing on water surface.

6. Conclusion

This paper presents a new design of a CDV, which can navigate across the water and air. The CDV can glide on water surface and take off rapidly. There are three advantages over traditional HAUVs. Firstly, the combination of air propeller and water jet propeller not only ensures the flexibility of surface sailing, but also greatly increases the maximum speed of surface navigation. Secondly, two sets of hydrofoils are added below the fuselage. These hydrofoils can not only improve the CDV's speed on surface for rapid gliding off but also reduce the impact on the CDV's fuselage when it lands on the water. Finally, two sets of foldable tandem airfoils can achieve larger lift and load capacity, and increase the possibility of CDV performing missions in narrow waters.

Different approaches including theoretical modeling, numerical simulation and experiments are applied to verify the feasibility of the proposed design. The dynamic models of low-speed sailing, high-speed sailing and glide-off of the CDV are established in this study. In these models, key parameters such as the position changes of the gravity center and buoyancy center of the CDV are discussed. Based on the conceptual design, the structure and control system of the CDV are designed in detail. In order to evaluate the advantages of hydrofoil, the cross-domain process of the CDV is studied by numerical simulation. By comparing the motion attitude of the CDV with or without hydrofoil, it is proved that hydrofoil can effectively improve the stability of the CDV, rapidly lift the body and effectively reduce the navigation resistance. In addition, the surface landing of the CDV is also evaluated numerically. The results show that the hydrofoil can effectively reduce the overload of the fuselage during landing. Finally, a proof-of-concept prototype named "QianXiang II" was fabricated and tested. The cross-domain navigation experiment was carried out on the lake, and the feasibility of the CDV was proved by the whole cross-domain cycle of low-speed sailing, steering, high-speed sailing, glide-off, air flight and landing on water surface.

There are still lots of works to be done to improve the present design. More innovative design of the CDV structure is needed to enable underwater navigation, meanwhile more detailed aerodynamics/hydrodynamics analysis and optimization of the CDV is also required to further improve the cross-domain capability of the CDV.

CRediT authorship contribution statement

Yucheng Zou: designed the vehicle, All authors have read and agreed to the published version of the manuscript. **Chenxi You:** analyzed the simulation, Formal analysis, All authors have read and agreed to the published version of the manuscript. **Xiangkui Tan:** designed the vehicle, All authors have read and agreed to the published version of the manuscript. **Yiwei Wang:** provided the idea, All authors have read and agreed to the published version of the manuscript. **Jingzhu Wang:** analyzed the simulation, Formal analysis, All authors have read and agreed to the published version of the manuscript. **Chaohui Li:** analyzed the simulation, Formal analysis, All authors have read and agreed to the published version of the manuscript. **Ming He:** edited and proofread the article, Writing – review & editing, All authors have read and agreed to the published version of the manuscript. **Kai Lv:** wrote the paper, All authors have read and agreed to the published version of the manuscript. **Yong Zou:** analyzed the simulation, Formal analysis, All authors have read and agreed to the published version of the manuscript. **Huaitong Song:** wrote the paper, All authors have read and agreed to the published version of the manuscript. **Pengyu Lv:** edited and proofread the article, Writing – review & editing, All authors have read and agreed to the published version of the manuscript. **Hongyuan Li:** provided the idea, All authors have read and agreed to the published version of the manuscript.
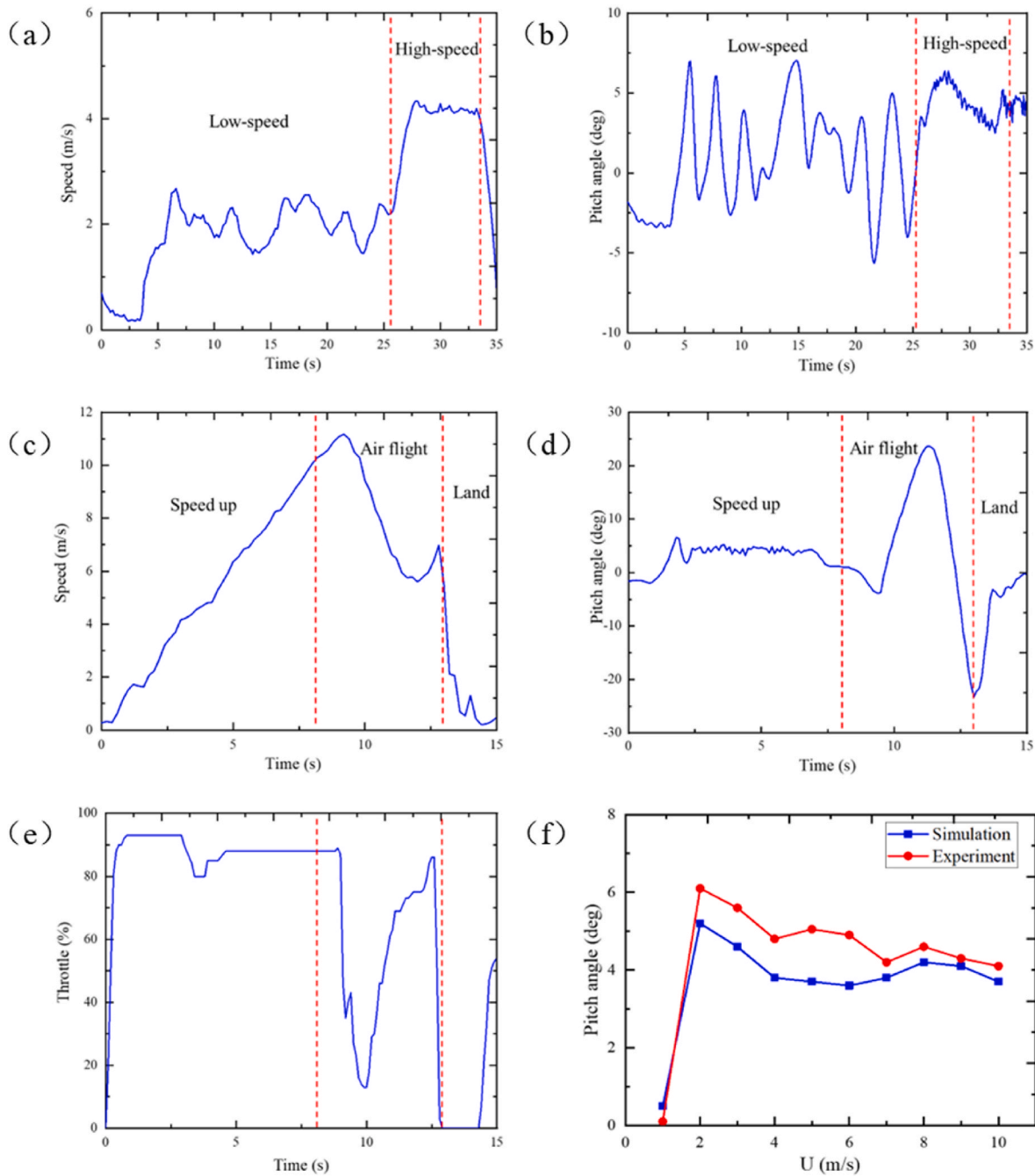
Fig. 17. The test results of CDV's motion attitude in the cross-domain process. (a) Horizontal speed of water navigation; (b) pitch angle of water navigation; (c) horizontal speed of cross-domain process; (d) pitch angle of cross-domain process; (e) throttle of cross-domain process; (f) comparison of experiment and simulation.

Declaration of competing interest

The authors declare that they have no known competing financial interests or personal relationships that could have appeared to influence the work reported in this paper.

Data availability

Data will be made available on request.

Appendix

The following abbreviations are used in this manuscript:

Variable	Description
r	The linear moving vector along the global coordinate axis
Ω	The rotation angle vector along the global coordinate axis
δ	The angle of rotation along the x axis of the global coordinate system
θ	The angle of rotation along the y axis of the global coordinate system
φ	The angle of rotation along the z axis of the global coordinate system
CG	Mass center of vehicle
HF	Buoyancy center of vehicle
G	Total gravity of the vehicle system
F_B	Buoyancy of the vehicle
F_R	Resistance of the vehicle, which includes both in air and water
P_W	Water jet thrust at the tail of the vehicle
α	Angle between lift coefficient and drag coefficient of hydrofoil
F_{L1}	The resultant drag and lift of the front hydrofoil
F_{L2}	The resultant drag and lift of the rear hydrofoil
U	The speed of the vehicle in global coordinates , $U = (U_x, U_y, U_z)$
$\dot{U}_x$	The acceleration of the vehicle along the x axis in the global coordinate system
$\dot{U}_z$	The acceleration of the vehicle along the z axis in the global coordinate system
L_y	The rotational inertia of the vehicle system along the y axis
$\ddot{\theta}$	Angular acceleration about the Y-axis
P_A	The pull of the air propeller
m_i	The total mass of the vehicle itself and the water around it
m	The mass of the vehicle itself
H	Diameter of vehicle body
d	Maximum submergence depth of vehicle in water
λ_i	Additional mass coefficient of vehicle
γ	The angle between lift coefficient and drag coefficient of main airfoil
D_1	The resultant drag and lift of the front airfoil
D_2	The resultant drag and lift of the rear airfoil
β	The Angle between lift coefficient and drag coefficient of airfoil aileron
T_1	The resultant lift and drag of the front ailerons
T_2	The resultant lift and drag of the rear ailerons
M_B	Torque due to different positions of buoyancy center and mass center
M_{PA}	Torque caused by propeller tension
M_{L1}	Torque caused by the lift and drag of the front hydrofoil
M_{L2}	Torque caused by the lift and drag of the rear hydrofoil
M_{D1}	Torque caused by lift and drag of the front airfoil
M_{D2}	Torque caused by lift and drag of the rear airfoil
M_{T1}	Torque caused by lift and drag of front ailerons
M_{T2}	Torque caused by lift and drag of rear ailerons

Appendix A. Supplementary data

Supplementary data to this article can be found online at https://doi.org/10.1016/j.oceaneng.2023.114549.

References

Anderson, K.L., Blankenship, G.L., Lebow, L.G., 1988. A rule-based adaptive PID controller. Proceedings of the 27th IEEE conference on decision and control 564–569.

Barbarino, S., Bilgen, O., Ajaj, R.M., Friswell, M.I., 2011. A review of morphing aircraft. J. Intell. Mater. Syst. Struct. 22 (9), 823–877.

Cui, W.C., 2018. An overview of submersible research and development in China. J. Mar. Sci. Appl. 17 (4), 459–470.

Drews, P., L, J., Neto, A.A., Campos, M., F, M., 2014. Hybrid unmanned aerial underwater vehicle: modeling and simulation. IEEE Int. Conf. Intell. Robots Syst. 4637–4642.

Duan, X., Sun, W., Chen, C., Wei, M., Yang, Y., 2018. Numerical investigation of the porpoising motion of a seaplane planing on water with high speeds. Aero. Sci. Technol. 247 (1), 1–15.

FLITETEST, 2018. The flying submarine story. http://www.flitetest.com.

Gao, A., Techet, A.H., 2011. Design considerations for a robotic flying fish. In: OCEANS'11 MTS/IEEE KONA, pp. 1–8.

Guo, Y., Ma, D., Yang, M., Liu, X., 2021. Numerical analysis of the T ake-off performance of a seaplane in calm water. Appl. Sci. 11, 6442.

He, M., Wang, S., Ren, S., Zhang, S., 2021. Numerical study of effects of stand-off distance and gravity on large scale bubbles near a breach. Appl. Ocean Res. 117, 102946.

Horn, A.C., Pinheiro, P.M., Grando, R.B., Silva, C.B., Neto, A., Drews-Jr, P.L.J., 2020. A Novel Concept for Hybrid Unmanned Aerial Underwater Vehicles Focused on Aquatic Performance. 2020 Latin American Robotics Symposium (LARS), 2020

Brazilian Symposium on Robotics (SBR) and 2020 Workshop on Robotics in Education (WRE), pp. 1–6.

Hu, J., Xu, B., Feng, J., Qi, D., Yang, J., Wang, C., 2017. Research on water-exit and take-off process for morphing unmanned submersible aerial vehicle. China Ocean Eng. 31 (2), 202–209.

Jia, D., Zou, Y.C., Pang, F.Z., Miao, X.H., Li, H.C., 2022. Experimental study on the characteristics of flow-induced structure noise of underwater vehicle. Ocean. Eng. 262, 112126.

Lou, J.K., Wang, H.D., Wang, J.Y., Cai, Q., Yi, H., 2022. Deep learning method for 3-DOF motion prediction of unmanned surface vehicles based on real sea maneuverability test. Ocean. Eng. 250.

Lyu, C.X., Lu, D., Xiong, C.K., Hu, R., Jin, Y.F., Wang, J.H., Zeng, Z., Lian, L., 2022. Toward a gliding hybrid aerial underwater vehicle: design, fabrication, and experiments. J. Field Robot. 39 (5), 543–556.

Maia, M.M., Mercado, D.A., Diez, F.J., 2017. Design and implementation of multirotor aerial-underwater vehicles with experimental results. Ieee Int. Confer. Robot. Syst. 961–966.

Mercado, D.A., Maia, M.M., Diez, F.J., 2017. Aerial-underwater systems, a new paradigm in unmanned vehicles. In: International Conference on Unmanned Aircraft System, pp. 1690–1695.

Moore, J., Fein, A., Setzler, W., 2018. Design and analysis of a fixed-wing unmanned aerial-aquatic vehicle. IEEE International Conference on Robotics and Automation (ICRA) 1237–1243.

Ozturk, U., Akdag, M., Ayabakan, T., 2022. A review of path planning algorithms in maritime autonomous surface ships: navigation safety perspective. Ocean. Eng. 251.

Park, D., 2015. A study on the effect of flat plate friction resistance on speed performance prediction of full scale. Int. J. Nav. Archit. Ocean Eng. 7 (1), 195–211.

Ravell, D., A, M., Maia, M.M., Diez, F.J., 2018. Modeling and control of unmanned aerial/underwater vehicles using hybrid control. Control Eng. Pract. 76, 112–122.

Ravenna, R., Song, S., Shi, W., Sant, T., Muscatfenech, C., D, M., Tezdogan, T., Demirel, Y.K., 2022. CFD analysis of the effect of heterogeneous hull roughness on ship resistance. Ocean. Eng. 258, 111733.

Ross, J., Lindsay, J., Gregson, E., Moore, A., Patel, J., Seto, M., 2019. Collaboration of multi-domain marine robots towards above and below-water characterization of floating targets. IEEE Int. Symp. Robot. Sens. Environ. 50–56.

Siddall, R., Ancel, A.O., Kovac, M., 2017. Wind and water tunnel testing of a morphing aquatic micro air vehicle. Interface Focus 7 (1).

Stewart, W., Weisler, W., MacLeod, M., Powers, T., Defreitas, A., Gritter, R., Anderson, M., Peters, K., Gopalarathnam, A., Bryant, M., 2018. Design and demonstration of a seabird-inspired fixed-airfoil hybrid UAV-UUV system. Bioinspiration Biomimetics 13 (5).

Stewart, W., Weisler, W., Anderson, M., Bryant, M., Peters, K., 2020. Dynamic modeling of passively draining structures for aerial-aquatic unmanned vehicles. J. Ocean. Eng. 45 (3), 840–850.

Tan, Y.H., Chen, B.M., 2019. Design of a Morphable Multirotor Aerial-Aquatic Vehicle. OCEANS 2019 MTS/IEEE SEATTLE, pp. 1–8.

Tan, Y.H., Chen, B.M., 2020. A morphable aerial-aquatic quadrotor with coupled symmetric thrust vectoring. IEEE International Conference on Robotics and Automation (ICRA) 2223–2229.

Tang, K.S., Man, K.F., Chen, G., Kwong, S., 2001. An optimal fuzzy PID controller. IEEE Trans. Ind. Electron. 48 (4), 757–765.

Villegas, A., Mishkevich, V., Gulak, Y., Diez, F.J., 2017. Analysis of key elements to evaluate the performance of a multirotor unmanned aerial-aquatic vehicle. Aero. Sci. Technol. 70, 412–418.

Wei, Z., Teng, Y., Meng, X., Yao, B., Lian, L., 2022. Lifting-principle-based design and implementation of fixed-airfoil unmanned aerial-underwater vehicle. J. Field Robot. 39 (6), 694–711.

Weisler, W., Stewart, W., Anderson, M.B., Peters, K.J., Gopalarathnam, A., Bryant, M., 2018. Testing and characterization of a fixed airfoil cross-domain unmanned vehicle operating in aerial and underwater environments. J. Ocean. Eng. 43 (4), 969–982.

Weisshaar, T.A., 2013. Morphing aircraft systems: historical perspectives and future challenges. J. Aircraft 50 (2), 337–353.

Wen, J., Zhang, W., Ren, L., Bao, L., Dini, D., Xi, H., Hu, H., 2020. Controlling the number of vortices and torque in Taylor–Couette flow. J. Fluid Mech. 901, 301–316.

Wynn, R.B., Huvenne, V., I, A., Bas, T.P.L., Murton, B.J., Connelly, D.P., Bett, B.J., Ruhl, H.A., Morris, K.J., Peakall, J., Parsons, D.R., Sumner, E.J., Darby, S.E., Dorrell, R.M., Hunt, J.E., 2014. Autonomous Underwater Vehicles (AUVs): their past, present and future contributions to the advancement of marine geoscience. Mar. Geol. 352, 451–468.

Yao, H., Qin, R.J., Chen, X.Y., 2019. Unmanned aerial vehicle for remote sensing applications-A review. Rem. Sens. 11 (12).

Yu, P., Xie, H., Liu, F., Li, P., Lv, G., 2022. Numerical investigation on the water entry of a 2D seaplane section with heel angles. Ocean. Eng. 262, 112236.

Zeng, Z., Lyu, C.X., Bi, Y.B., Jin, Y.F., Lu, D., Lian, L., 2022. Review of hybrid aerial underwater vehicle: cross-domain mobility and transitions control. Ocean. Eng. 248.

Zhou, X., Yuan, S., Yu, C., Li, H., Yuan, X., 2022. Performance comparison of feature Detectors on various layers of underwater acoustic imagery. J. Mar. Sci. Eng. 101601.

Zhou, H., Hu, K., Mao, L., Sun, M., Cao, J., 2023. Research on planing motion and stability of amphibious aircraft in waves based on cartesian grid finite difference method. Ocean. Eng. 272, 113848.

Zufferey, R., Ancel, A.O., Raposo, C., 2019. SailMAV: design and implementation of a novel multi-modal flying sailing robot. IEEE Rob. Autom. Lett. 4 (3), 2894–2901.